

www.acsami.org Research Article

Strong Interfacial Coupling of Tunable Ni-NiO Nanocomposite Thin Films Formed by Self-Decomposition

Xuejing Wang, Zhimin Qi, Juncheng Liu, Haohan Wang, Xiaoshan Xu, Xinghang Zhang, and Haiyan Wang*



Cite This: ACS Appl. Mater. Interfaces 2021, 13, 39730-39737



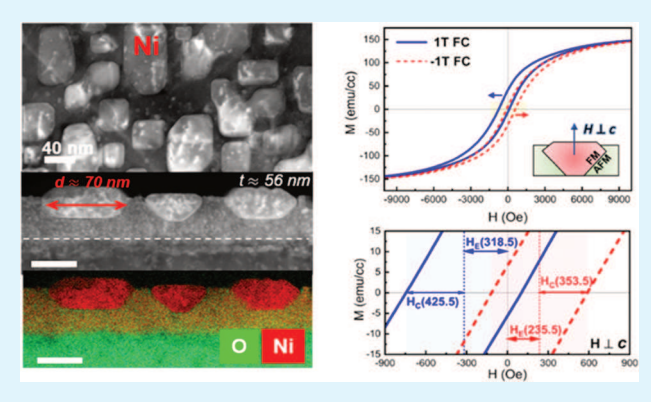
ACCESS

III Metrics & More

Article Recommendations

s Supporting Information

ABSTRACT: The next-generation spintronic devices including memristors, tunneling devices, or stochastic switching exert surging demands on magnetic nanostructures with novel coupling schemes. Taking advantage of a phase decomposition mechanism, a unique Ni–NiO nanocomposite has been demonstrated using a conventional pulsed laser deposition technique. Ni nanodomains are segregated from NiO and exhibit as faceted "emerald-cut" morphologies with tunable dimensions affected by the growth temperature. The sharp interfacial transition between ferromagnetic (002) Ni and antiferromagnetic (002) NiO, as characterized by high-resolution transmission electron microscopy, introduces a strong exchange bias effect and magneto-optical coupling at room temperature. *In situ* heating—cooling X-ray diffraction (XRD) study



confirms an irreversible phase transformation between Ni and NiO under ambient atmosphere. Synthesizing highly functional two-phase nanocomposites with a simple bottom-up self-assembly via such a phase decomposition mechanism presents advantages in terms of epitaxial quality, surface coverage, interfacial coupling, and tunable nanomagnetism, which are valuable for new spintronic device implementation.

KEYWORDS: exchange bias effect, magneto-optical coupling, tunable nanodomains, ferromagnetic anisotropy, optical anisotropy

■ INTRODUCTION

Interfacial coupling between two functional materials has enabled a wide variety of unprecedented physical phenomena that are promising for microelectronic and optical devices. 1-3 Exchange bias effect, as an example, is attributed to the exchange anisotropy generated between the ferromagnetic (FM) and antiferromagnetic (AFM) interface, represented by a shift of the hysteresis loop upon field cooling. 4-6 Since the first demonstration of exchange bias and magnetic anisotropy in Co-CoO core-shell nanoparticles,7 there have been extensive explorations in coupling different material candidates and geometries. 8-13 These functional materials with the exchange bias effect find promising applications in magnetic storage reader or writer designs, spin valve, and tunneling devices. 14-17 Recent studies have demonstrate that such FM-AFM nanostructures can generate spin—orbit torque (SOT) for memristors or function as an active element for neuromorphic spintronics. 18,19

Toward the realization of new spintronics devices, solid-state fabrication techniques including nanolithography and thin-film deposition produce reliable and durable materials. Among the conventional synthesis methods, chemical or solution-based growth techniques pave the way for extensive morphological tuning of functional nanostructures, ^{20–23} while physical

methods, such as pulsed laser deposition (PLD) technique, have demonstrated its unique advantages in fabricating vertically aligned FM-AFM nanocomposites (VANs) that possess perpendicular exchange bias effect. For example, FM lanthanum strontium manganite (La_{1-x}Sr_xMnO₃ or LSMO) perovskite oxide has been coupled with AFM oxides such as NiO, BiFeO₃, and LaFeO₃. ²⁴⁻²⁶ Such self-assembly process is realized by the variations of nucleation property between the two constituent phases, i.e., the matrix phase favors the layered growth mode while the pillar phase favors the islanded growth mode.^{27–29} The vertically aligned cylindrical nanopillars can be well coupled with the matrix phase, the aspect ratio and density can be tailored by varying the growth parameters or the target ratio, and so do their magnetic properties and exchange bias coupling properties.³⁰ Most of these two-phase nanocomposite systems involve either cogrowth of two different oxides^{31,32} or

Received: May 27, 2021 Accepted: July 30, 2021 Published: August 11, 2021





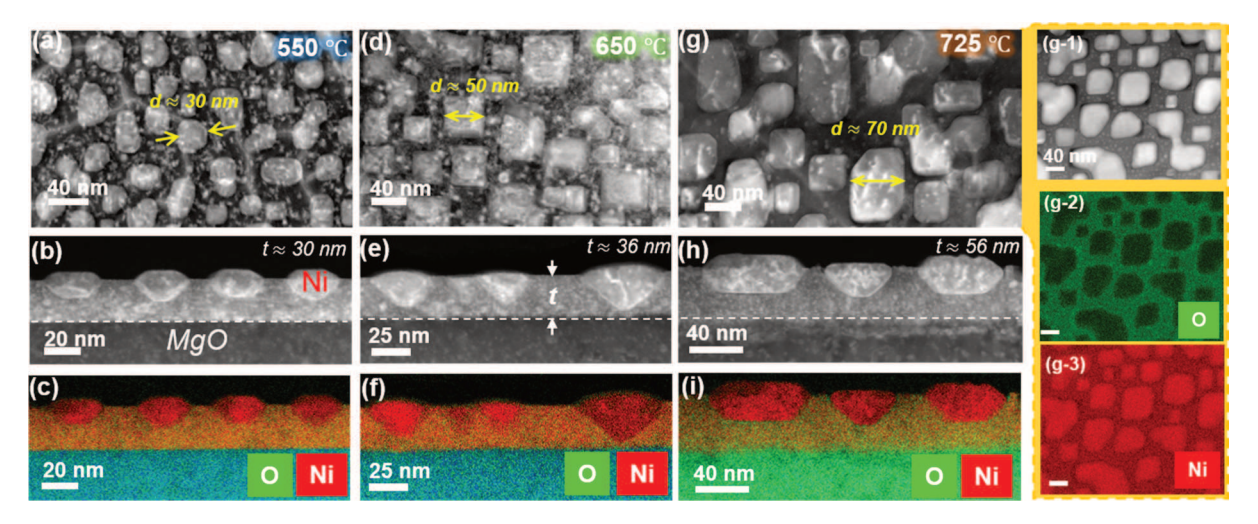


Figure 1. (a) Plan-view STEM (b, c) cross-sectional STEM micrographs and EDX mapping of the Ni–NiO film grown at 550 °C. (d) Plan-view STEM (e, f) cross-sectional STEM micrographs and EDX mapping of the Ni–NiO film grown at 650 °C. (g) Plan-view STEM (h, i) cross-sectional STEM micrographs and EDX mapping of the Ni–NiO film grown at 725 °C. Red: Ni; Green: O. (g-1)–(g-3) Plan-view STEM micrograph and EDX mapping of the Ni–NiO film grown at 725 °C.

codeposition of a metal with an oxide, ^{28,33} which are often limited by materials compatibility and chemical stability.

In this study, an epitaxial metal-oxide (Ni-NiO) FM-AFM nanocomposite has been demonstrated. Different from the previous reported Ni-NiO core-shell nanostructures fabricated by methods such as hydrothermal or sputtering,^{34–37} here, a self-decomposition thin-film growth mechanism is applied where the Ni phase is segregated from the NiO matrix as an "emerald-cut" domain geometry, possessing desirable output scale and epitaxial quality. Such well-coupled nanostructures are expected to present a strong exchange bias effect at room temperature (RT). A similar decomposition mechanism has been reported in a La_{0.5}Sr_{0.5}FeO₃ system, where α -Fe nanowires were segregated under reduced oxygen pressure.³⁸ Key findings in this work include the wellsegregated two-phase epitaxy resulted from the unique growth mechanism, tunable domain morphology, and the effective change of magnetic and optical anisotropies, as well as magneto-optical coupling and exchange bias effect from the strongly coupled Ni/NiO. These findings demonstrate the power of this Ni-NiO nanocomposite system toward potential spintronic devices and nanophotonic applications.

■ RESULTS AND DISCUSSION

To realize the as-proposed two-phase nanocomposites, the PLD growth was conducted under high vacuum condition, using a pure NiO target. Three deposition temperatures (550, 650, and 725 °C) were tested, and the corresponding morphologies are displayed in Figure 1. Both cross-section (Figure 1b,e,h) and plan-view (Figure 1a,d,g) scanning transmission electron microscopy (STEM) micrographs indicate a clear phase contrast between the two phases, i.e., saturated domains with the brighter contrast contain a higher Ni concentration, according to the energy-dispersive X-ray spectroscopy (EDX) mapping (Figure 1c,f,i). Corresponding X-ray diffraction (XRD) scans (Figure S1) of films grown at three growth temperatures confirm the out-of-plane (OP) epitaxial relationship as $(002)_{N_i}||(002)_{N_i}||(002)_{M_0}||$. From the zoomed θ –2 θ scans (Figure S1b,c), there is no obvious shift of the major peaks. For the 725 °C film, the full width at halfmaximum (FWHM) value of the Ni (002) peak is slightly

higher, which is confirmed by a more desirable crystallinity or homogeneity of the growth according to the top projection STEM images (Figure 1g-1–g-3). The morphological change along with the increase of temperature indicates a gradual increase of the Ni nanodomain size and the overall film thickness, which can be explained as thermal energy facilitated nucleation and growth. The average domain sizes of Ni, as calculated from the plan-view STEM micrographs, are 36.3 nm (550 °C), 46.0 nm (650 °C), and 61.3 nm (725 °C), respectively.

Interestingly, Ni nanodomains exhibit as well-faceted emerald-cut-like geometries. Besides these major nanodomains, there are ultrafine Ni clusters (Figure S2) that belong to the unsaturated phase segregation in the process of coalescence. To elucidate the potential formation mechanism, we conducted the growth under 10 mTorr O₂ and found that all of the emerald-cut-like nanodomains disappeared (data not shown), leaving densely packed ultrafine Ni dots dispersed throughout the film. This indicates that the formation of this specific Ni-NiO morphology is very sensitive to the background pressure. From Figure 1b,e,h, it is noticed that the phase segregation only starts from the middle of the growth, which is affected by both strain and thermal energy. As illustrated in Figure S3, a three-stage self-decomposition mechanism is proposed for the Ni-NiO nanocomposite growth. In the first stage, NiO adatoms being ablated from the target are nucleated on the MgO substrate with a close lattice match (\approx 1.00%). Due to the reduced oxygen pressure, Ni tends to segregate from NiO and forms ultrafine clusters. Next, thermal energy facilitates the coalescence of Ni clusters, forming emerald-cut nanodomains. In the third stage, the phase segregation is gradually stabilized, and the final domain size is affected by the growth temperature. Fundamentally, the self-decomposition mechanism generally requires a complex oxide that favors composition fluctuation (i.e., cation or cation oxide segregation) under controlled processing conditions (e.g., background pressure, temperature, chemical composition).³⁹ Studies have shown that the diffusion coefficient of Al in Al₂O₃, O in CoO, Cu in Cu₂O, Ni in NiO, and Mg in MgO are highly sensitive to the change of both temperature and oxygen pressure. 40 The chemical reaction $2\text{NiO} \leftrightarrow 2\text{Ni} + \text{O}_2$

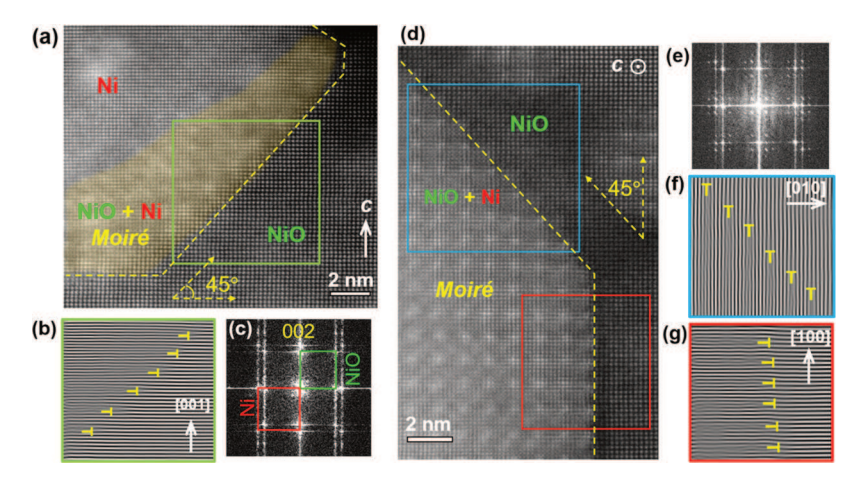


Figure 2. (a) Cross-sectional HRSTEM micrograph at the Ni/NiO interface (650 °C), the shaded area indicates moiré fringes affected by the lattice interference between NiO (002) and Ni (002). (b) IFFT-filtered Ni/NiO interface with edge dislocations (6:5) marked in yellow. (c) Local DPs. Red: Ni; green: NiO. (d) Plan-view HRSTEM micrograph. (e) Corresponding local DPs showing moiré diffraction. Corresponding IFFT-filtered Ni/NiO interfacial areas (d) along (f) [010] and (g) [100] direction, exhibiting a 6 Ni (002):5 NiO (002) stacking periodicity.

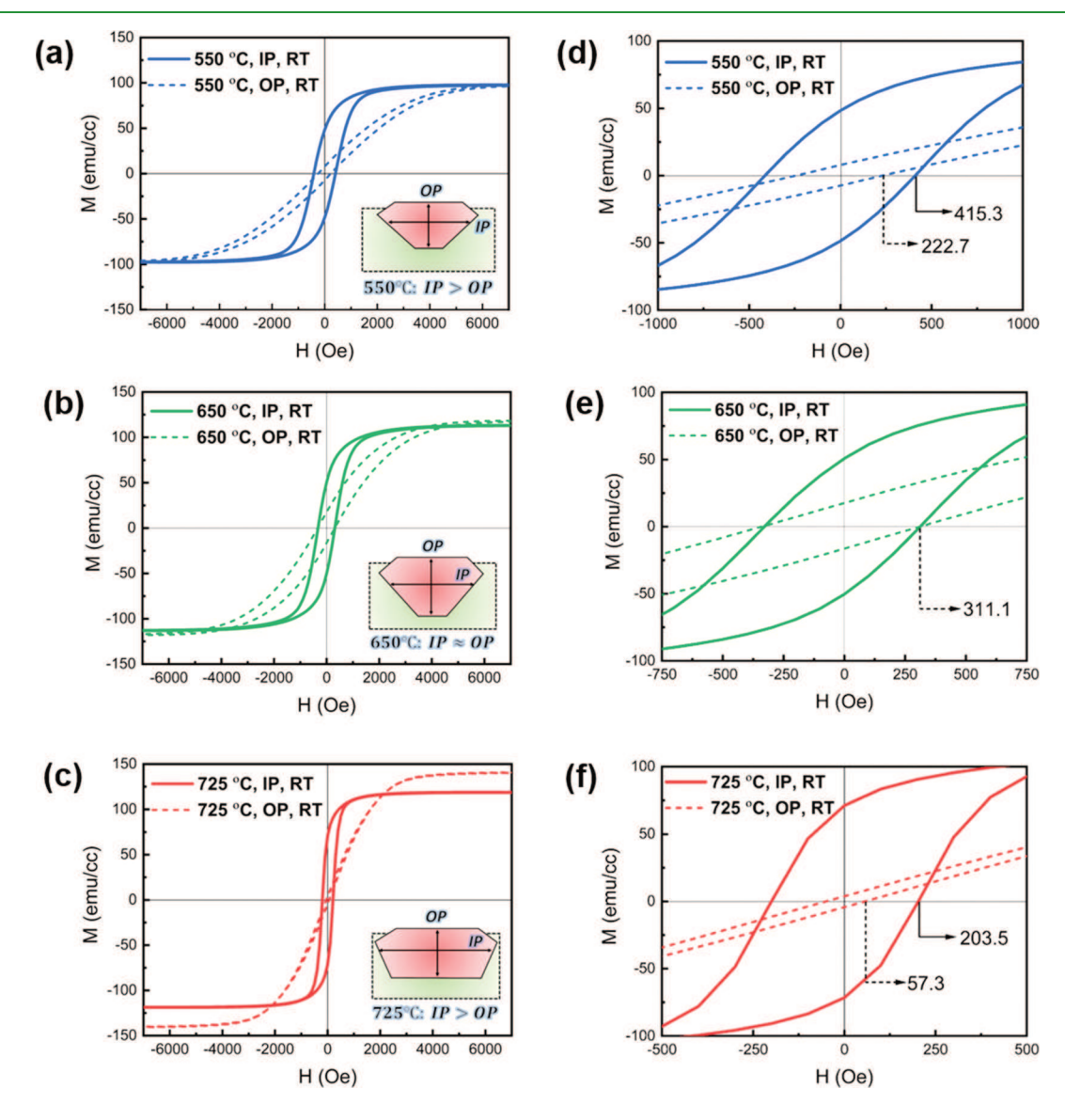


Figure 3. Magnetic hysteresis loops of three Ni–NiO films grown under (a) 550 °C, (b) 650 °C, and (c) 725 °C. Inset images compare the unit cell geometry, i.e., the relative dimension between the Ni nanodomain and the NiO matrix. (d–f) Enlarged displays of M–H at three temperatures; H_C values are marked out.

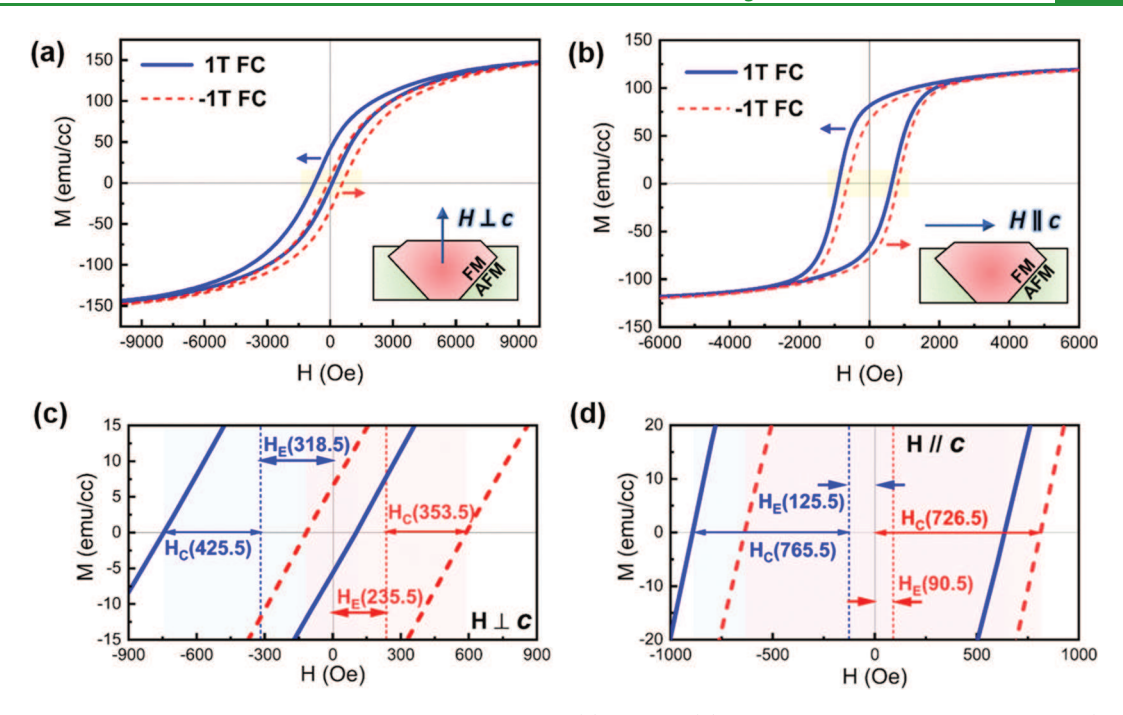


Figure 4. Exchange bias property from the 650 °C grown Ni–NiO film. (a) OP and (b) IP M–H loops upon 1T field cooling (blue solid) and -1T field cooling (red dashed). Insets show the structural illustration. Zoomed loops showing H_E and H_C values of (c) OP and (d) IP M–H.

indicates the formation of Ni upon reduced oxygen atmosphere, which is one of the main reasons that NiO is selected for this study.

Focusing at the Ni/NiO interface (the 650 °C film) as displayed in Figure 2, the Ni-NiO coupling results in a singlecrystalline stacking between Ni (002) and NiO (002). From cross-sectional high-resolution STEM (HRSTEM) (Figure 2a) micrographs, a transition (yellow shaded) region with translational moiré fringes is clearly observed, which is caused by a parallel superposition between NiO (002) and Ni (002) lattices without any rotation. Interestingly, the edge of Ni nanodomains along c-axis stacking follows roughly a 45° sequence, which can be correlated with its growth temperature and surface energy. The local diffraction patterns (DPs) from the imaged area provide clear evidence of cube-on-cube matching relation between Ni (002) and NiO (002), which is consistent with the XRD θ -2 θ scans. Similar observations are found in the plan-view HRSTEM, where moiré fringes are visualized at the entire Ni phase due to the overlap from top projection, corresponding DPs present satellite patterns that confirm the moiré diffraction. Based on the plan-view and cross-sectional STEM micrographs in Figure 1, several major findings are noted. First, with the increase of growth temperature, nanodomain facets become more obvious, from curved edges (Figure 1a) at 550 °C to square-like edges (Figure 1g) at 725 °C. In addition, more lateral elongation is observed, which means the exposure of 45° planes (the highenergy (110) surface) are reduced. 41 Further, three interfacial areas (marked by colored boxes in Figure 2a,d) are selected to apply the fast Fourier transform (FFT). According to the inverse FFT (IFFT) along [001] (b), [010] (f), and [100] (g) orientations, edge dislocations at the Ni/NiO interface follow the same periodicity, i.e., six Ni (002) atomic planes versus five NiO (002) atomic planes, which matches well with the 19.853% strain according to the XRD results.

Since the Ni segregation introduces a ferromagnetic phase in the nanocomposite, magnetic hysteresis (M–H) loops of the

Ni-NiO films grown at three temperatures were collected and the results are displayed in Figure 3. It is obvious that the temperature-induced morphological change plays a role in tuning magnetic properties, including magnetic anisotropy (i.e., in-plane (IP) vs out-of-plane (OP) responses), coercive field (H_C) , and magnetic saturation (M_S) . The Ni-NiO unit cells (Figure 3a-c) are illustrated to help explain the magnetic performance. As explained earlier, along with the increase of temperature, the overall domain size keeps increasing for all three films. The Ni nanodomains nucleated at 650 °C exhibit comparable lateral and vertical dimensions, while for 550 and 725 °C films, the nanodomains appear wider lateral elongations. Affected by the morphological variations, the M_S value keeps increasing along the IP direction, correlated with the lateral elongation of FM nanodomains under higher temperature. To visualize H_C intersections, M-H plots are enlarged, as shown in Figure 3d-f. Compare to the hysteresis loop of the 650 °C film $(H_{\rm C}^{\rm IP} \approx H_{\rm C}^{\rm OP})$, loops from the other two films exhibit higher anisotropy, with H_C^{IP}/H_C^{OP} values of approximately 1.86 (550 °C) and 3.55 (725 °C), respectively. The difference between H_C^{IP} and H_C^{OP} can be explained by the ratio between the lateral and vertical dimensions of the Ni nanodomains.

To test the exchange bias behavior at the Ni/NiO interface, magnetic hysteresis was measured under the 1T and -1T field cooling (FC) for the film grown at 650 °C (Figure 4a,b). Figure 4c,d displays the enlarged view. From both IP and OP directions, the loops exhibit obvious lateral shifts at room temperature, which suggests an FM/AFM coupling at the Ni/NiO interface. Such exchange bias effect can be correlated with the moiré fringes due to an overlapping feature between Ni (002) and NiO (002). It is predicted that the exchange biasing can be further enhanced if the moiré region is enlarged. Specifically, under 1T FC, the exchange bias value ($H_{\rm E}$) from OP (318.5 Oe) is higher than that of IP (125.5 Oe), indicating a stronger spin-torque being exerted from the vertical direction with changes of the magnetic field. Compared with regular M—

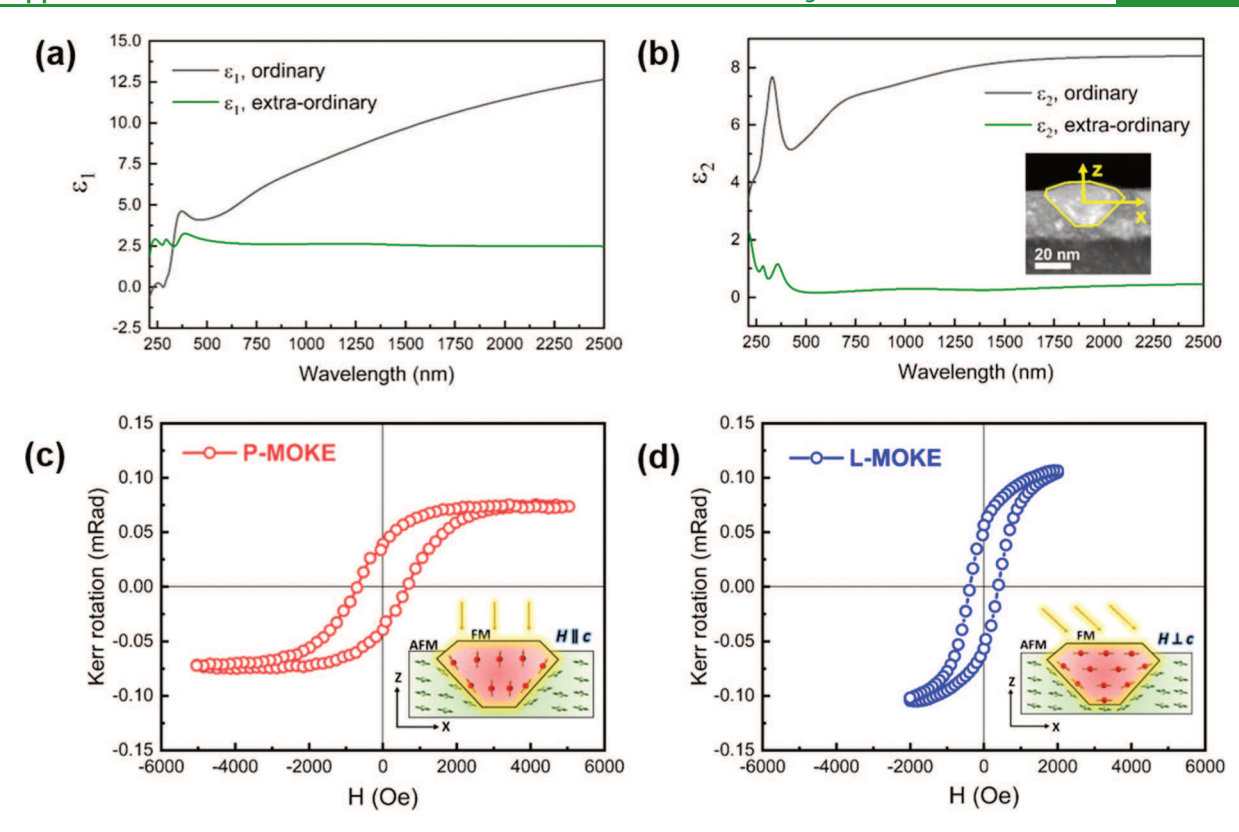


Figure 5. (a) Real part and (b) imaginary part dielectric function of the 650 $^{\circ}$ C film, the ordinary component corresponds to x or y directions, and the extra-ordinary component corresponds to the z-direction. (c) P-MOKE and (d) L-MOKE Kerr loops of the Ni–NiO film grown at 650 $^{\circ}$ C. Insets illustrate the spin polarization upon laser beam excitation for two MOKE configurations.

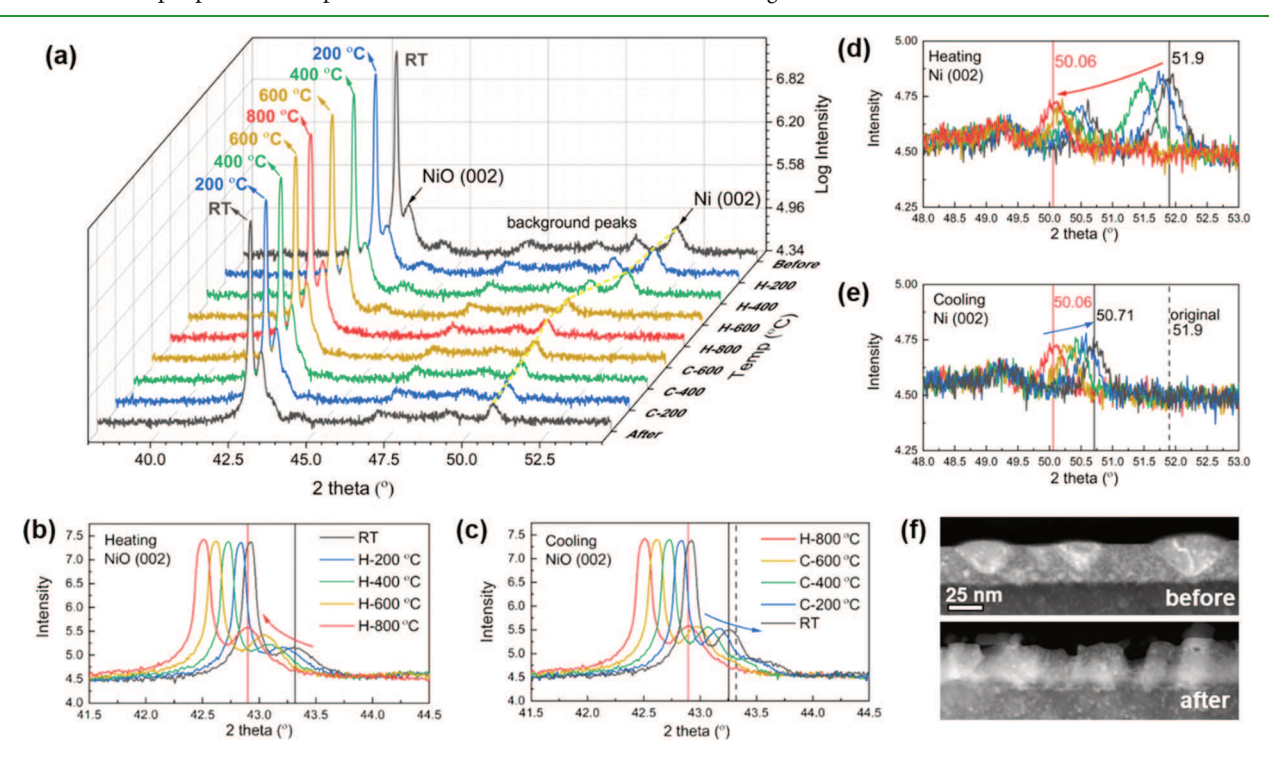


Figure 6. In situ heating XRD of the Ni–NiO film grown at 650 °C. (a) Stacked θ –2 θ scans of the heating–cooling cycle (RT to 800 °C at ambient atmosphere). (b) Heating and (c) cooling 2 θ profiles at 41.5–44.5°, corresponding to the NiO (002) peak. (d) Heating and (e) cooling 2 θ profiles at 48.0–53.0°, corresponding to the Ni (002) peak. (f) Cross-sectional STEM micrographs comparing film morphologies before (two-phase) and after heating (mixed phase).

H with $H_{\rm C}$ of 311.1 Oe, the prealigned spins under field cooling generally enlarge the $H_{\rm C}$ as marked in Figure 4c,d.

On the other hand, the plasmonic resonance of Ni nanoparticles located at around 450 nm⁴² suggests a potential

electromagnetic wave excitation of localized surface plasmon resonance (LSPR) mode at the nanodomain interface. It could also be interesting to explore the optical anisotropy introduced by emerald-cut-like Ni nanostructures. The dielectric constant retrieved from a uniaxial model based on Gen-Osc oscillators confirms such anisotropy. Figure 5a,b displays the real (ε_1) and imaginary part (ε_2) dielectric tensors for the Ni-NiO film grown under 650 °C. The drastic difference between the ordinary (IP) and extra-ordinary (OP) tensors indicate a strong optical anisotropy upon light-matter interaction; meanwhile, Ohmic losses $(\varepsilon_2 > 0)$ contributed by the metallic Ni phase have been observed. Figure S4 couples the uniaxial ε_1 tensors of three different films; all films exhibit effective dielectric response ($\varepsilon_1 > 0$). A comparison between IP and OP dielectric tensors indicate a more metallic nature along the OP direction $(\varepsilon_1^{\rm O} > \varepsilon_1^{\rm EO})$, such anisotropy becomes more obvious at a higher wavelength. Additionally, the fitted reflectance (R) spectra (Figure S4d-S4f) show a slightly enhanced intensity for films grown under higher temperatures, which is potentially caused by stronger electromagnetic wave interaction along the wide lateral nanodomains. LSPR of Ni nanostructures is represented by the oscillations at low wavelength range (210-750 nm).

Furthermore, such nanoscale light-matter interaction could be coupled with the ferromagnetic property. Therefore, magneto-optical Kerr effect (MOKE) was measured in this system by collecting the room-temperature Kerr rotation upon changing the magnetic field with two configurations, i.e., P-MOKE with both laser and magnetic field oscillating perpendicularly with respect to the film surface (H||c), and L-MOKE with laser impinges at 30° while magnetic field being parallel to the film surface $(H \perp c)$. The resulted hysteresis loops indicate a strong anisotropic magneto-optical coupling. Compare to P-MOKE (Figure 5c), the L-MOKE loop (Figure 5d) shows a smaller H_C while a higher saturation of Kerr rotation, which indicates a stronger light-matter interaction when the incident light impinges along 30° and exhibits a higher coincidence with the 45° Ni/NiO interface. Detailed schematic illustrations are shown as insets. It is proposed that the spin canting at the Ni/NiO interface upon the applied magnetic field is potentially enhanced by the LSPR mode (shaded yellow) of Ni. Similar tunable MO coupling induced by nanoferromagnets has been reported previously.4

Since the formation of the Ni-NiO nanocomposite is resulted from the NiO reduction under high temperature without introducing any oxygen flow, it is interesting to explore the thermal stability as well as the phase transformation reversibility of the system. Therefore, in situ XRD heating experiments under ambient atmosphere were performed by running a heating-cooling cycle from RT to 800 °C. According to the stacked θ -2 θ scans (Figure 6a), films remain with high crystallinity without forming new peaks or the disappearance of existing peaks. It is noted that peaks located in the range of 46-50° belong to the background noise and will not be discussed here. From the results, two sections corresponding to Ni (002) and NiO (002) are selected, and their θ -2 θ scans during heating and cooling are displayed separately in Figure 6b-e. When heating from RT to 800 °C, both phases experience a thermal expansion which is represented by a left shift of their (002) peaks, from 43.255 to 42.895° for NiO (002) (0.83%) while from 51.9 to 50.06° for Ni (002) (3.55%), respectively. Such changes are affected by the coefficient of thermal expansion (CTE) and the

sensitivity to the background pressure. Interestingly, the intensity of NiO (002) is increased while the intensity is reduced for Ni (002), indicating the phase transformation of $2Ni + O_2 \rightarrow 2NiO$. Upon cooling from 800 °C to RT, while NiO (002) almost retrieves to its original (43.32°) position, Ni (002) shifts to 50.71°, which causes a 2.29% variation. There is no obvious intensity change upon cooling, which indicates both phases are stabilized without further phase transformation. In addition, cross-sectional microstructures for the films before and after the heating-cooling cycle are presented in Figures 6f and S5. Once cooled to RT, the emerald-cut Ni nanodomains no longer exist, which confirms the chemical reaction (Ni \rightarrow NiO) with the presence of oxygen. Still, there are remaining Ni ultrafine clusters, which explains the existence of the low-intensity Ni (002) peak. It is expected that the exchange bias effect could be significantly reduced in the heated sample without Ni/NiO domain coupling.

For most of the metal-oxide and FM-AFM nanocomposites reported previously, complex processing steps are typically required starting from the mixture of two material components. Thus, factors such as immiscibility, cation size, lattice, and crystal symmetry are important for the materials selections. Here, the self-decomposition growth mechanism allows the two-phase segregation using one oxide target, which simplifies the processing steps and material selections, and realizes an ideal interfacial coupling between the two phases. Despite that the core-shell nanostructures using chemical synthesis methods can present versatile geometries, 46 such nanostructures have limitations for solid-state device applications due to their limited thermal and mechanical durability. Another advantage of this method is that many other potential metal-oxide systems such as Al-Al₂O₃, Cu-Cu₂O₃, or Fe-Fe₂O₃ or Co-CoO nanocomposites can be explored, as Al, Cu, Fe, and Co exhibit tremendous potentials in low-loss plasmonics and tunable ferromagnetism. 47 Meanwhile, these metal-oxide nanocomposite systems should be able to sustain thermal fluctuations under vacuum conditions. However, there are remaining challenges that need to be resolved. For example, improving the homogeneity of such segregation by fully activate the phase transformation through post processing, so that those ultrafine Ni particles can be completely transformed into the saturated nanodomains. It could be expected that by vacuum annealing, the thermal energy can facilitate the equilibrium of such phase transformation process, potentially results in more uniform segregation of nanodomains. Device implementation toward magnetic tunnel junction, surface plasmon-enhanced photocatalytic sensors and devices can be explored in the future studies.

CONCLUSIONS

The phase decomposition mechanism in forming selfassembled Ni-NiO nanocomposite thin films presents valuable insights into fabricating hybrid two-phase nanocomposite systems via a relatively simple and effective way. The segregated Ni nanodomains exhibit a periodic domain matching relationship with the NiO matrix as 6 Ni (002):5 NiO (002). Translational moiré fringes confirm a superior cube-on-cube epitaxial coupling between the two phases. Temperature-dependent morphological changes are correlated with magnetic properties, which demonstrate a tunable FM anisotropy attributed to the aspect ratio of the Ni nanodomains. The Ni-NiO film surface is optically active as represented by the strong room-temperature MO coupling as

well as anisotropic dielectric tensors. Coupled with the exchange bias effect at the FM-AFM interface, the presented functional heterostructures open enormous possibilities as new hybrid metamaterial designs toward next-generation spintronic devices.

■ EXPERIMENTAL SECTION

Sample Fabrication. The Ni–NiO thin-film nanocomposites were grown on MgO (001) substrates using the pulsed laser deposition (PLD) system (Neocera, Lambda PHysik Compex Pro 205, KrF excimer laser, λ = 248 nm). Pure NiO (99.9%) target was synthesized by the conventional sintering process using NiO powders. Growth was conducted under high vacuum with a base pressure of 2.0 × 10⁻⁶ mbar. The laser beam was focused onto the NiO target at 45° incident angle. Three temperatures (550, 650, and 725 °C) and a laser frequency of 5 Hz were applied. After the growth, the chamber was cooled at 15 °C/min under vacuum.

Microstructure Characterization. X-ray diffraction experiments including 2θ and *in situ* heating were carried on a Panalytical X'Pert diffractometer with Cu K α radiation. High-angle annular dark-field (HAADF) STEM micrographs were collected on an aberration-corrected FEI Themis Z microscope; EDX chemical mapping was conducted on an FEI Talos F200X TEM. The TEM specimens were prepared using the conventional mechanical method, including grinding, dimpling, and ion milling (PIPS 691).

Optical Characterization. Ellipsometry measurements were carried on an RC2 spectroscopic ellipsometer (J. A. Woollam Company). Parameters including amplitude and phase difference parameters were collected at 55, 65, and 75° incident angles. The uniaxial model was built using Gen-Osc oscillators (Cody-Lorentz and Tauc Lorentz) to fit dielectric constant with Kramers—Kronig consistency. The mean square error (MSE) is below 3.

Magnetic and Kerr Measurements. Magnetic hysteresis loops (with and without field cooling) were collected using a magnetic property measurement system (MPMS) from Quantum Design. Vibrating sample magnetometer (VSM) mode with a superconducting quantum interference device (SQUID) sensor was applied for high accuracy. A home-built magneto-optical Kerr effect (MOKE) system with a He–Ne laser at 632.8 nm was used for room-temperature Kerr measurements. The incident light was polarized using a linear polarizer, and the Kerr rotation was measured using a second polarizer assisted by a photoelastic modulator. For polar configuration, the reflected light was separated from the normal incident light by a 50% beam splitter, with a magnetic field perpendicular to the film surface. For longitudinal mode, the laser impinged at approximately 30° incidence, and the magnetic field was parallel to the film surface.

■ ASSOCIATED CONTENT

Supporting Information

The Supporting Information is available free of charge at https://pubs.acs.org/doi/10.1021/acsami.1c09793.

XRD θ - 2θ scans, illustrations of self-decomposition growth mechanism, fitted dielectric function and reflectance spectra corresponding to the three Ni-NiO films grown at different temperatures, and microstructure and EDX mapping of the film after the *in situ* XRD heating-cooling cycle (PDF)

AUTHOR INFORMATION

Corresponding Author

Haiyan Wang — School of Materials Engineering, Purdue University, West Lafayette, Indiana 47907, United States; School of Electrical and Computer Engineering, Purdue University, West Lafayette, Indiana 47907, United States; orcid.org/0000-0002-7397-1209; Email: hwang00@purdue.edu

Authors

Xuejing Wang — School of Materials Engineering, Purdue University, West Lafayette, Indiana 47907, United States Zhimin Qi — School of Materials Engineering, Purdue University, West Lafayette, Indiana 47907, United States Juncheng Liu — School of Materials Engineering, Purdue

Juncheng Liu – School of Materials Engineering, Purdue University, West Lafayette, Indiana 47907, United States

Haohan Wang – Department of Physics and Astronomy, University of Nebraska-Lincoln, Lincoln, Nebraska 68588, United States

Xiaoshan Xu — Department of Physics and Astronomy, University of Nebraska-Lincoln, Lincoln, Nebraska 68588, United States; o orcid.org/0000-0002-4363-392X

Xinghang Zhang — School of Materials Engineering, Purdue University, West Lafayette, Indiana 47907, United States; orcid.org/0000-0002-8380-8667

Complete contact information is available at: https://pubs.acs.org/10.1021/acsami.1c09793

Notes

The authors declare no competing financial interest.

ACKNOWLEDGMENTS

X.W. and H.W. acknowledge the funding support from U.S. National Science Foundation, DMR-2016453 for thin-film processing and DMR-1565822 for the high-resolution STEM imaging effort. H.H.W. and X.X. acknowledge the support from U.S. National Science Foundation, DMR-1454618.

REFERENCES

- (1) Pan, Z.; Yao, L.; Zhai, J.; Yao, X.; Chen, H. Interfacial Coupling Effect in Organic/Inorganic Nanocomposites with High Energy Density. *Adv. Mater.* **2018**, *30*, No. 1705662.
- (2) Kim, K.-W.; Lee, K.-J.; Sinova, J.; Lee, H.-W.; Stiles, M. D. Spin-Orbit Torques from Interfacial Spin-Orbit Coupling for Various Interfaces. *Phys. Rev. B* **2017**, *96*, No. 104438.
- (3) Tan, S.; Argondizzo, A.; Ren, J.; Liu, L.; Zhao, J.; Petek, H. Plasmonic Coupling at a Metal/Semiconductor Interface. *Nat. Photonics* **2017**, *11*, 806–812.
- (4) Nogués, J.; Schuller, I. K. Exchange Bias. J. Magn. Magn. Mater. 1999, 192, 203–232.
- (5) Nogués, J.; Sort, J.; Langlais, V.; Skumryev, V.; Suriñach, S.; Muñoz, J. S.; Baró, M. D. Exchange Bias in Nanostructures. *Phys. Rep.* **2005**, *422*, 65–117.
- (6) Stamps, R. L. Mechanisms for Exchange Bias. J. Phys. D: Appl. Phys. 2000, 33, R247-R268.
- (7) Meiklejohn, W. H.; Bean, C. P. New Magnetic Anisotropy. *Phys. Rev.* **1956**, *102*, 1413–1414.
- (8) Dho, J.; Qi, X.; Kim, H.; MacManus-Driscoll, J. L.; Blamire, M. G. Large Electric Polarization and Exchange Bias in Multiferroic Bifeo3. *Adv. Mater.* **2006**, *18*, 1445–1448.
- (9) González, J. A.; Andrés, J. P.; López Antón, R.; De Toro, J. A.; Normile, P. S.; Muñiz, P.; Riveiro, J. M.; Nogués, J. Maximizing Exchange Bias in Co/Coo Core/Shell Nanoparticles by Lattice Matching between the Shell and the Embedding Matrix. *Chem. Mater.* **2017**, *29*, 5200–5206.
- (10) Sun, X.; Frey Huls, N.; Sigdel, A.; Sun, S. Tuning Exchange Bias in Core/Shell Feo/Fe3o4 Nanoparticles. *Nano Lett.* **2012**, *12*, 246–251
- (11) Nogués, J.; Lederman, D.; Moran, T. J.; Schuller, I. K. Positive Exchange Bias in Fef2-Fe Bilayers. *Phys. Rev. Lett.* **1996**, *76*, 4624–4627.

- (12) Ali, M.; Adie, P.; Marrows, C. H.; Greig, D.; Hickey, B. J.; Stamps, R. L. Exchange Bias Using a Spin Glass. *Nat. Mater.* **2007**, *6*, 70–75.
- (13) Stiles, M. D.; McMichael, R. D. Coercivity in Exchange-Bias Bilayers. *Phys. Rev. B* **2001**, *63*, No. 064405.
- (14) Li, K.; Wu, Y.; Guo, Z.; Zheng, Y.; Han, G.; Qiu, J.; Luo, P.; An, L.; Zhou, T. Exchange Coupling and Its Applications in Magnetic Data Storage. *J. Nanosci. Nanotechnol.* **2007**, *7*, 13–45.
- (15) Wei, Z.; Sharma, A.; Nunez, A. S.; Haney, P. M.; Duine, R. A.; Bass, J.; MacDonald, A. H.; Tsoi, M. Changing Exchange Bias in Spin Valves with an Electric Current. *Phys. Rev. Lett.* **2007**, *98*, No. 116603.
- (16) Anderson, G.; Huai, Y.; Miloslawsky, L. Cofe/Irmn Exchange Biased Top, Bottom, and Dual Spin Valves. *J. Appl. Phys.* **2000**, *87*, 6989–6991.
- (17) Jiang, Y.; Nozaki, T.; Abe, S.; Ochiai, T.; Hirohata, A.; Tezuka, N.; Inomata, K. Substantial Reduction of Critical Current for Magnetization Switching in an Exchange-Biased Spin Valve. *Nat. Mater.* **2004**, *3*, 361–364.
- (18) Grollier, J.; Querlioz, D.; Camsari, K. Y.; Everschor-Sitte, K.; Fukami, S.; Stiles, M. D. Neuromorphic Spintronics. *Nat. Electron.* **2020**, *3*, 360–370.
- (19) Kurenkov, A.; Fukami, S.; Ohno, H. Neuromorphic Computing with Antiferromagnetic Spintronics. *J. Appl. Phys.* **2020**, *128*, No. 010902.
- (20) Hassanpour, M.; Salavati-Niasari, M.; Tafreshi, S. A. H.; Safardoust-Hojaghan, H.; Hassanpour, F. Synthesis, Characterization and Antibacterial Activities of Ni/Zno Nanocomposites Using Bis(Salicylaldehyde) Complex Precursor. *J. Alloys Compd.* **2019**, 788, 383–390.
- (21) Gholami, T.; Salavati-Niasari, M.; Varshoy, S. Electrochemical Hydrogen Storage Capacity and Optical Properties of Nial2o4/Nio Nanocomposite Synthesized by Green Method. *Int. J. Hydrogen Energy* **2017**, *42*, 5235–5245.
- (22) Ranjeh, M.; Ghiyasiyan-Arani, M.; Slavati-Niasari, M.; Moayedi, H. Li4zn3b4o11/Li2b2o4 Nanocomposites as a Potential Electrode Material for Electrochemical Hydrogen Storage; Insight of Fabrication and Morphology Controlling. *J. Mater. Res. Technol.* **2020**, *9*, 2028–2036
- (23) Najafian, H.; Manteghi, F.; Beshkar, F.; Salavati-Niasari, M. Enhanced Photocatalytic Activity of a Novel Nio/Bi2o3/Bi3clo4 Nanocomposite for the Degradation of Azo Dye Pollutants under Visible Light Irradiation. Sep. Purif. Technol. 2019, 209, 6–17.
- (24) Zhang, W.; Li, L.; Lu, P.; Fan, M.; Su, Q.; Khatkhatay, F.; Chen, A.; Jia, Q.; Zhang, X.; MacManus-Driscoll, J. L.; Wang, H. Perpendicular Exchange-Biased Magnetotransport at the Vertical Heterointerfaces in La0.7sr0.3mno3:Nio Nanocomposites. ACS Appl. Mater. Interfaces 2015, 7, 21646–21651.
- (25) Zhang, W.; Chen, A.; Jian, J.; Zhu, Y.; Chen, L.; Lu, P.; Jia, Q.; MacManus-Driscoll, J. L.; Zhang, X.; Wang, H. Strong Perpendicular Exchange Bias in Epitaxial La0.7sr0.3mno3:Bifeo3 Nanocomposite Films through Vertical Interfacial Coupling. *Nanoscale* **2015**, *7*, 13808–13815.
- (26) Chen, A.; Wang, Q.; Fitzsimmons, M. R.; Enriquez, E.; Weigand, M.; Harrell, Z.; McFarland, B.; Lü, X.; Dowden, P.; MacManus-Driscoll, J. L.; Yarotski, D.; Jia, Q. Hidden Interface Driven Exchange Coupling in Oxide Heterostructures. *Adv. Mater.* 2017, 29, No. 1700672.
- (27) Chen, A.; Bi, Z.; Jia, Q.; MacManus-Driscoll, J. L.; Wang, H. Microstructure, Vertical Strain Control and Tunable Functionalities in Self-Assembled, Vertically Aligned Nanocomposite Thin Films. *Acta Mater.* **2013**, *61*, 2783–2792.
- (28) Wang, X.; Wang, H. Self-Assembled Nitride—Metal Nanocomposites: Recent Progress and Future Prospects. *Nanoscale* **2020**, 12, 20564—20579.
- (29) Misra, S.; Wang, H. Review on the Growth, Properties and Applications of Self-Assembled Oxide—Metal Vertically Aligned Nanocomposite Thin Films—Current and Future Perspectives. *Mater. Horiz.* **2021**, *8*, 869–884.

- (30) Wang, X.; Wang, H.; Jian, J.; Rutherford, B. X.; Gao, X.; Xu, X.; Zhang, X.; Wang, H. Metal-Free Oxide-Nitride Heterostructure as a Tunable Hyperbolic Metamaterial Platform. *Nano Lett.* **2020**, 20, 6614–6622.
- (31) Huang, J.; MacManus-Driscoll, J. L.; Wang, H. New Epitaxy Paradigm in Epitaxial Self-Assembled Oxide Vertically Aligned Nanocomposite Thin Films. *J. Mater. Res.* **2017**, *32*, 4054–4066.
- (32) Chen, A.; Su, Q.; Han, H.; Enriquez, E.; Jia, Q. Metal Oxide Nanocomposites: A Perspective from Strain, Defect, and Interface. *Adv. Mater.* **2019**, *31*, No. 1803241.
- (33) Zhang, D.; Wang, H. Self-Assembled Metal—Dielectric Hybrid Metamaterials in Vertically Aligned Nanocomposite Form with Tailorable Optical Properties and Coupled Multifunctionalities. *Adv. Photonics Res.* **2021**, *2*, No. 2000174.
- (34) You, W.; Che, R. Excellent Nio-Ni Nanoplate Microwave Absorber Via Pinning Effect of Antiferromagnetic-Ferromagnetic Interface. ACS Appl. Mater. Interfaces 2018, 10, 15104-15111.
- (35) Yao, X.-J.; He, X.-M.; Song, X.-Y.; Ding, Q.; Li, Z.-W.; Zhong, W.; Au, C.-T.; Du, Y.-W. Enhanced Exchange Bias and Coercivity Arising from Heterojunctions in Ni–Nio Nanocomposites. *Phys. Chem. Chem. Phys.* **2014**, *16*, 6925–6930.
- (36) Bai, Y.; Yang, B.; Zhang, H.; Wu, X.; Jiang, N.; Zhao, S. Multi–Interface Spin Exchange Regulated Biased Magnetoelectric Coupling in Cluster–Assembled Multiferroic Heterostructural Films. *Acta Mater.* **2018**, *155*, 166–174.
- (37) Ting, Y.-H.; Chen, J.-Y.; Huang, C.-W.; Huang, T.-K.; Hsieh, C.-Y.; Wu, W.-W. Observation of Resistive Switching Behavior in Crossbar Core—Shell Ni/Nio Nanowires Memristor. *Small* **2018**, *14*, No. 1703153.
- (38) Mohaddes-Ardabili, L.; Zheng, H.; Ogale, S. B.; Hannoyer, B.; Tian, W.; Wang, J.; Lofland, S. E.; Shinde, S. R.; Zhao, T.; Jia, Y.; Salamanca-Riba, L.; Schlom, D. G.; Wuttig, M.; Ramesh, R. Self-Assembled Single-Crystal Ferromagnetic Iron Nanowires Formed by Decomposition. *Nat. Mater.* **2004**, *3*, 533–538.
- (39) MacManus-Driscoll, J. L. Self-Assembled Heteroepitaxial Oxide Nanocomposite Thin Film Structures: Designing Interface-Induced Functionality in Electronic Materials. *Adv. Funct. Mater.* **2010**, *20*, 2035–2045.
- (40) Barsoum, M. W. Fundamentals of Ceramics, 2003.
- (41) Vitos, L.; Ruban, A. V.; Skriver, H. L.; Kollár, J. The Surface Energy of Metals. Surf. Sci. 1998, 411, 186–202.
- (42) Chen, J.; Albella, P.; Pirzadeh, Z.; Alonso-González, P.; Huth, F.; Bonetti, S.; Bonanni, V.; Åkerman, J.; Nogués, J.; Vavassori, P.; Dmitriev, A.; Aizpurua, J.; Hillenbrand, R. Plasmonic Nickel Nanoantennas. *Small* **2011**, *7*, 2341–2347.
- (43) Bonanni, V.; Bonetti, S.; Pakizeh, T.; Pirzadeh, Z.; Chen, J.; Nogués, J.; Vavassori, P.; Hillenbrand, R.; Åkerman, J.; Dmitriev, A. Designer Magnetoplasmonics with Nickel Nanoferromagnets. *Nano Lett.* **2011**, *11*, 5333–5338.
- (44) Oppeneer, P. M.; Maurer, T.; Sticht, J.; Kübler, J. Ab Initio Calculated Magneto-Optical Kerr Effect of Ferromagnetic Metals: Fe and Ni. *Phys. Rev. B* **1992**, *45*, 10924–10933.
- (45) Maccaferri, N.; Berger, A.; Bonetti, S.; Bonanni, V.; Kataja, M.; Qin, Q. H.; van Dijken, S.; Pirzadeh, Z.; Dmitriev, A.; Nogués, J.; Åkerman, J.; Vavassori, P. Tuning the Magneto-Optical Response of Nanosize Ferromagnetic Ni Disks Using the Phase of Localized Plasmons. *Phys. Rev. Lett.* **2013**, *111*, No. 167401.
- (46) Ghosh Chaudhuri, R.; Paria, S. Core/Shell Nanoparticles: Classes, Properties, Synthesis Mechanisms, Characterization, and Applications. *Chem. Rev.* **2012**, *112*, 2373–2433.
- (47) Jiang, Q.; Ji, C.; Riley, D. J.; Xie, F. Boosting the Efficiency of Photoelectrolysis by the Addition of Non-Noble Plasmonic Metals: Al & Cu. *Nanomaterials* **2019**, *9*, No. 1.